A new $n = 4$ Ruddlesden-Popper phase $K_{2.5}Bi_{2.5}Ti_4O_{13} \cdot H_2O$ showing reversible stoichiometric hydration at 110 °C

Liu, S.,[*,†] Avdeev, M.,[‡] Liu, Y.,[¶] Johnson, M.R.,[§] and Ling, C.D.[†]

†*School of Chemistry, University of Sydney, Sydney 2006, Australia*

‡*The Bragg Institute, ANSTO, PMB 1, Menai 2234, Australia*

¶*Research School of Chemistry, Australian National University, ACT 2601, Australia*

§*Institute Laue Langevin, F-38042 Grenoble, France*

E-mail: samuel.liu@sydney.edu.au

Abstract

A new highly ordered Bi-containing layered perovskite of the Ruddlesden-Popper phase, $K_{2.5}Bi_{2.5}Ti_4O_{13}$, has been prepared by solid state synthesis. It has been shown to hydrate to form stoichiometric $K_{2.5}Bi_{2.5}Ti_4O_{13} \cdot H_2O$. Diffraction data show that the structure consists of a quadruple stacked ($n = 4$) perovskite layer with K-ions occupying the rock salt layer and its next-nearest A-site. The hydrated sample was shown to remove the offset between stacked perovskite layers relative to the dehydrated sample. Computational methods show that the hydrated phase consists of intact water molecules in a vertical "pillared" arrangement bridging across the interlayer space. Rotations of water molecules about the *c*-axis were evident in molecular dynamic calculations, which increased in rotation angle with increasing temperature. *In situ* diffraction data point to a broad structural phase transition consistent with relaxor behaviour from orthorhombic to tetragonal at T_C ~600 °C. A corresponding

broad increase in the dielectric constant was observed in dielectric property measurements. The relative Bi-rich composition in the perovskite block results in a higher T_C compared to related perovskite structures. Water makes a significant contribution to the dielectric constant, which disappears after dehydration.

Introduction

Naturally layered perovskite-type materials, in which perovskite-type $[A_{n-1}B_nO_{3n+1}]$ blocks n-layers thick alternate with "spacer" layers of another structure type, offer an interesting structural framework for combining normally disparate physical properties. Layered perovskites have been extensively studied as potential dielectrics (e.g., ferroelectric applications[1,2]), magnetic materials (e.g. colossal magnetoresistors[3]), superconductors,[4–7] multiferroics,[8–10] photocatalytics,[11–15] ionic conductors[16] and for their intercalation chemistry.[17–19] In some cases, specific properties are enhanced in layered structures for example, the layered perovskites $Sr_4Ti_3O_{10}$ and $Sr_3Ti_2O_7$ offer markedly higher activity of H_2 production from photoexcitation compared to the pure perovskite $SrTiO_3$ due to their ability to readily uptake water in interlayer gaps.[14,15]

The three most studied layered perovskites are the Dion-Jacobson (DJ),[20] Ruddlesden-Popper (RP),[21] and Aurivillius[22] phases, $A[A_{n-1}B_nO_{3n+1}]$, $A_2[A_{n-1}B_nO_{3n+1}]$, $[Bi_2O_2][A_{n-1}B_nO_{3n+1}]$ respectively, where $[A_{n-1}B_nO_{3n+1}]$ is the n layer-thick perovskite block. Differences in the nature of the "spacer layer" between perovskite blocks can have profound effects on their chemistry and properties. For example, the α-PbO-type $[Bi_2O_2]^{2+}$ layer in Aurivillius phases has stereochemically active electron lone pairs on Bi^{3+}, which produce structural distortions that increase B-site cation offsets and enhance ferroelectricity.[23–25] The opposite can be achieved by doping Sr^{2+} into the $[Bi_2O_2]^{2+}$ layer, essentially decreasing the effect (comparing distortion parameters between $Bi_2PbNb_2O_9$ and $Bi_2SrNb_2O_9$).[26]

For the DJ and RP phases, the interlayer atoms are commonly alkali salt cations, and their arrangement can allow or forbid ion exchange and intercalation of certain types of

molecules. In general, the DJ and RP phases differ by only one alkali cation in the empirical formula (A_1 vs A_2 respectively). The A_1 layer of DJ phases can either be offset in only one direction, or none at all, *i.e.*, $(\frac{1}{2}, 0, 0)$, $(0, \frac{1}{2}, 0)$ or $(0, 0, 0)$ when c is the stacking axis. The RP phase A_2 layer is stacked in a rock salt-type arrangement, such that the adjacent perovskite blocks are staggered by half a unit cell in a and b $(\frac{1}{2}, \frac{1}{2}, 0)$. These subtle differences have been shown to have a major effect on intercalation chemistry, with the $(\frac{1}{2}, \frac{1}{2}, 0)$ staggered arrangement of adjacent layers in RP phases not allowing for the intercalation of large organic bases compared to related DJ phases.[17]

Some RP phases have been shown to readily uptake water in the interlayer space, with potential applications for photocatalytic splitting of H_2O.[15] This causes an expansion in the stacking axis (usually c) and in some cases a structural transformation from *Immm* to *Pmmm* symmetry. The $(\frac{1}{2}, \frac{1}{2}, 0)$ offset is removed upon hydration and the uptake of water causes the adjacent perovskite blocks to eclipse above and below one another (something not generally observed in DJ phases).[27]

For the DJ and RP structure types, Bi-containing phases with thicker perovskite layers ($n > 3$) are rare with only one report to our knowledge on $KBi_3Ti_4O_{13}$ ($n = 4$)[28] and an $n = 5$ analogue containing Pb, both reported as DJ-type phases.[28,29] In the present work, we reproduce the synthesis of $KBi_3Ti_4O_{13}$ and show that it is actually an $n = 4$ RP phase of the formula $K_{2.5}Bi_{2.5}Ti_4O_{13}$. This is consistent with the reported hydration behaviour of "$KBi_3Ti_4O_{13}$",[28] which we also observe and fully characterise, giving the first detailed picture of the structure of the intercalated water in an RP phase.

Experimental Section

Three samples were synthesised by the solid state method: $KBi_3Ti_4O_{13}$ and $K_{2.5}Bi_{2.5}Ti_4O_{13}$ in stoichiometric ratios; and $KBi_3Ti_4O_{13}$ with 2 mol KNO_3-excess as per Gopalakrishnan *et al.*[28] A ∼15g sample of each was prepared by weighing stoichiometric amounts of KNO_3

(Fluka, > 99%), Bi_2O_3 (Aithaca, 99.999%, dried at 750 °C for 20 hours before use), and TiO_2 (Aithaca, 99.995%). A 2 mol KNO_3-excess was used in one $KBi_3Ti_4O_{13}$ preparation to test the suppression of the Aurivillius phase formation as suggested by previous authors.[28] The reagents were ground in acetone to a homogeneous powder with a mortar and pestle. The three mixtures were held in separate alumina crucibles and were heated to 750 °C for 8 hours twice in a muffle furnace with intermediate regrinding. Off-white coloured samples were obtained for the stoichiometrically prepared samples. The KNO_3-excess sample was washed with distilled water and dried at 110 °C for 24 hrs which yielded a light yellow powder. The polycrystalline products were analysed by X-ray powder diffraction (XRD) for purity and preliminary structure analysis. The samples were then exposed to a humid environment to form hydrated versions.

X-ray powder diffraction (XRD) was used to monitor the progress and purity of the reactions. XRD data were obtained using a PANalytical X'pert PRO diffractometer in Bragg-Brentano geometry using a sealed-tube source of Cu-K_α radiation ($\lambda_{\alpha 1}$ = 1.5405 Å, $\lambda_{\alpha 2}$ = 1.5443 Å). Data were collected in the range $5° \leq 2\theta \leq 80°$ with a step size of 0.1313°.

Thermogravimetric analysis was carried out on a TA instruments TGA 2950 machine. Approximately 10-20 mg of the hydrated sample were placed in the sample environment chamber at room temperature and increased above reaction temperatures at a heating rate of 2 °C/min.

Scanning electron microscopy (SEM) with energy dispersive X-ray (EDX) analysis were conducted at the Australian Microscopy and Microanalysis Research Facility (AMMRF) at the University of Sydney on a Zeiss EVO-50 Quemscan instrument equipped with a LaB_6 gun and an EDX detector. Samples were pelletised to provide a smooth surface and coated with 15 nm of carbon using an Emitech K550X sputter coater provided by the AMMRF. The incident wave energy was set at 20 kV, appropriate to overcome energy barriers for atomic edges, with a working distance ∼20 mm.

Synchrotron X-ray powder diffraction (SXRD) data were obtained at the Australian Syn-

chrotron on the Powder Diffraction beamline.[30] Samples were ground into very fine powders and placed in 0.3 mm quartz capillaries for high-temperature measurements, or 0.3 mm boron glass capillaries for room-temperature measurements. Data were collected in Debye-Scherrer geometry at 13000 eV. The corresponding wavelength refined against a LaB_6 NIST standard was $\lambda = 0.953296$ (1) Å. Data collection under non-ambient conditions was achieved using a hot air blower. The temperature range was controlled between room temperature and 900 °C (5-10 °C steps, 5 °C/min ramp) with 2 × 120 sec (2 detector positions) acquisition time at each step from $3^\circ \leq 2\theta \leq 83^\circ$.

Neutron powder diffraction (NPD) data were obtained at the Bragg Institute, Australian Nuclear Science and Technology Organisation (ANSTO), using the Echidna (high-resolution) diffractometer.[31] Powdered samples were sealed in 9 mm diameter vanadium cans and low-, high- and room-temperature data were collected between 100 K and 1173 K with 2 hour data collection at each step. A vacuum furnace was used for high-temperature measurements and a cryofurnace was used for low-temperature measurements. The cryofurnace gave an instrumental peak at 160° which was excluded from the refinements. Data were collected between $2.75^\circ \leq 2\theta \leq 164^\circ$ at a wavelength $\lambda = 1.6215$ Å.

Rietveld refinements against XRD, SXRD and NPD data were carried out using the GSAS[32] program with the EXPGUI[33] interface. Crystal structures were visualised using the VESTA software program.[34]

Ab initio geometry optimisations (GO) and molecular dynamics (MD) calculations were performed using density functional theory-based methods implemented in Vienna *Ab initio* Simulation Package (VASP) code.[35] Projector augmented wave (PAW) pseudopotentials[36] and the generalised gradient approximation Perdew-Burke-Ernzerhof (GGA-PBE)[37] functional were used. Sampling of the electronic structure in reciprocal space was performed at the gamma point. Molecular dynamics (MD) trajectories were visualised using the Large Array Manipulation Program (LAMP).[38]

Hydrated $K_{2.5}Bi_{2.5}Ti_4O_{13} \cdot H_2O$ powders were pressed into 13 mm diameter pellets and

their surfaces lightly polished using dry sand papers (1200 grit). Contact surfaces were carefully coated with gold using a DC sputtering instrument to achieve good electrical contact for electrical property measurements whilst keeping the hydration state of the samples. The dielectric properties were investigated in the intermediate frequency range of 300 Hz $\leq f \leq$ 500 kHz using a precision LCR metre (Agilent, E4980A) linked with a high-temperature dielectric measurement furnace. The dielectric properties of the fresh sample were measured first during the heating process up to 500 °C and on cooling to the room temperature. For higher tempertures (≥500 °C), the sample was polished to remove the gold electrode and re-coated using Pd-Ag alloy paste. It was then heat treated at 450 °C for 15 mins in order to remove any organic substrates and optimise electrical contact.

Results and Discussion

The compound investigated was previously identified as a DJ phase with hydration behaviour consistent with the RP-type structure.[28] A lack of Rietveld analysis in previous studies has motivated us to reinvestigate the nominal composition and structure of this $n = 4$ layered material. Of the synthetic scenarios tested, we found that Gopalakrishnan *et al.* were correct in that the formation of $KBi_3Ti_4O_{13}$ in stoichiometric amounts was not possible due to the overwhelming stability of the Aurivillius phase, $Bi_4Ti_3O_{12}$.[25] They proposed that the success of forming the layered phase was highly dependant on suppressing the formation of this Aurivillius phase with a large excess of K. However, we found that an $n = 4$ phase could be formed not only in the 2 mol K-excess condition, but also the stoichiometric $K_{2.5}Bi_{2.5}Ti_4O_{13}$ (which mimics a 1.5 mol K-excess rather than 2 mol K-excess scenario), previously reported as an unsuccessful synthetic route.[28] Figure 1 shows XRD patterns from samples reacted at these two different metal atom ratios. Both show peaks characteristic of the formation of an $n = 4$ layered phase, but the former also contains reflections of monoclinic α-Bi_2O_3 marked by asterisks (*). This suggests that the $n = 4$ phase composition is actually $K_{2.5}Bi_{2.5}Ti_4O_{13}$,

consistent with an RP phase rather than a DJ phase.

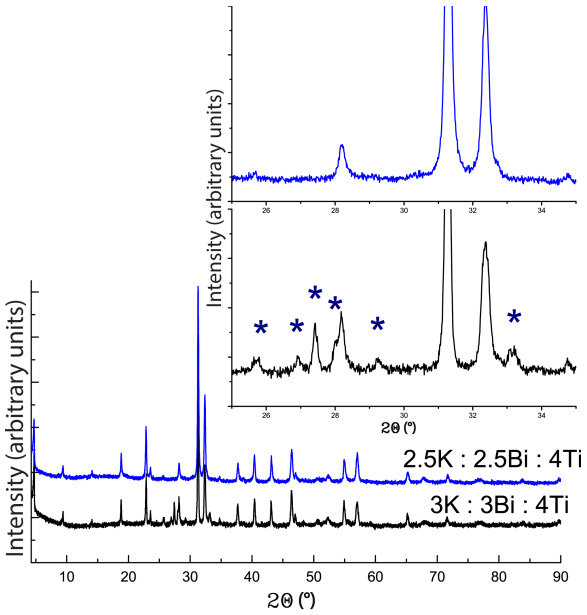

Figure 1: Laboratory XRD patterns of the tested synthetic scenarios. The top patterns (including inset) are of the stoichiometric 2.5K:2.5Bi:4Ti condition. The bottom patterns (including inset) are of the 3K:3Bi:4Ti (K-excess) condition used by previous authors. The K-excess condition shows marked Bi_2O_3 peaks with asterisks (*).

SEM-EDX results show a homogeneous surface for regions on a pellet of $K_{2.5}Bi_{2.5}Ti_4O_{13}$ with the backscattered electron (BSE) detector (Figure 2). Sampled EDX data collected were averaged with the multiple points and areas of collection. Mapped composition regions by EDX were normalised to four Ti atoms as shown in Table 1. The composition numbers show an almost perfect 1:1 ratio of K:Bi and no significant deviation from the 2.5K:2.5Bi:4Ti metal ratio, indicating minimal K-loss by evaporation. Overall, this suggests that the ratio of reagents in the 2 mol K-excess condition does not fulfil the stoichiometric ratio of the pure material. The chemical formula by these findings confirms the stoichiometric formula $K_{2.5}Bi_{2.5}Ti_4O_{13}$.

TGA was carried out on the hydrated sample $K_{2.5}Bi_{2.5}Ti_4O_{13} \cdot mH_2O$. Figure 3 shows an abrupt weight loss at approximately 110 °C, plateauing at higher temperatures. The ∼1.8% weight loss corresponds to one water molecule per formula unit, *i.e.*, $K_{2.5}Bi_{2.5}Ti_4O_{13} \cdot H_2O$. The fact that the dehydration temperature appears so low, suggests that the bonds formed

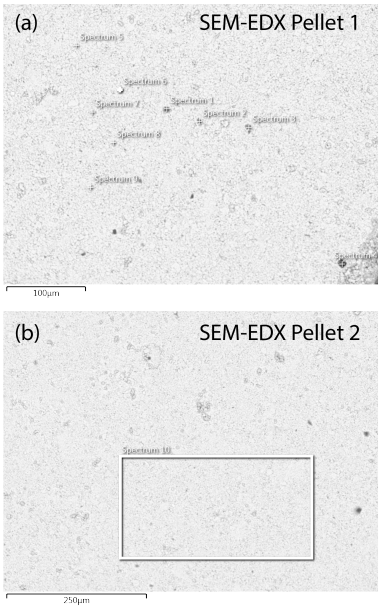

Figure 2: SEM-EDX image from the BSE detector of a pressed pellet of the material. Dark spots are graphite left from carbon coating. (a) is pin-point detection and (b) is the area mapped composition.

Table 1: Averaged metal compositions normalised over Ti extracted from EDX analysis.

Stoichiometric $K_{2.5}Bi_{2.5}Ti_4O_{13}$	Pellet 1	Pellet 2
K	2.427	2.409
Bi	2.437	2.446
Ti	4	4

between water and the crystal structure are relatively weak and that water mobility close to this temperature should therefore be relatively high.

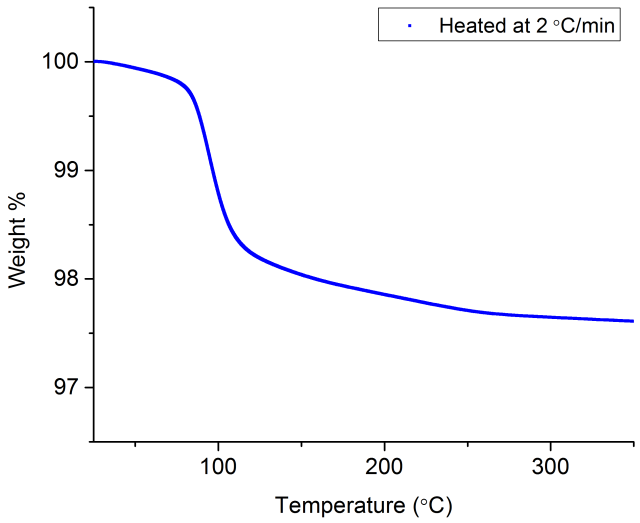

Figure 3: TGA measured at a rate of 2 °C/min showing an abrupt ∼1.8% weight loss corresponding to one water molecule per formula unit of $K_{2.5}Bi_{2.5}Ti_4O_{13}$.

Structural Analysis

The chemical results reported above indicate that the $n = 4$ formed by previous synthesis is an RP phase rather than a DJ phase. This was confirmed by Rietveld refinements against SXRD data. Our starting models used the *Immm* space group, commonly used to describe layered perovskite materials, specifically $Na_2Ca_2Nb_4O_{13}$.[39] However, a significant improvement in the fit was achieved by using the space group determined by single crystal analysis of $Na_2Ca_2Nb_4O_{13}$,[40] orthorhombic $Bb2_1m$ (non-standard setting of $Cmc2_1$, #36). Both space group models were tested by Rietveld refinement and a better goodness of fit statistic (χ^2) was achieved for $Bb2_1m$ as shown in Table 2. The accountability of allowed reflections, in particular ∼20° 2θ observed in high-resolution SXRD data is improved in the $Bb2_1m$ model over *Immm* (Supplementary Figure S1). Using a polar space group was also confirmed by a strong signal in the SHG measurements, which is available in Supplementary documents.

The zero offset, atomic positions, isotropic atomic displacement parameters (ADPs), lattice and profile parameters and metal occupancies were refined. The final refinement confirms that the 2.5K:2.5Bi:4Ti reactant ratio, *i.e.* $K_{2.5}Bi_{2.5}Ti_4O_{13}$, produced a pure sample with no obvious Bi_2O_3 impurity present.

Table 2: Fitting parameters extracted from SXRD Rietveld refinements. The higher resolution data provide a better fit for $Bb2_1m$ over $Immm$.

Parameter	$Bb2_1m$	$Immm$
χ^2	18.36	21.89
R_{wp}	0.0762	0.0832
R_p	0.0539	0.0573

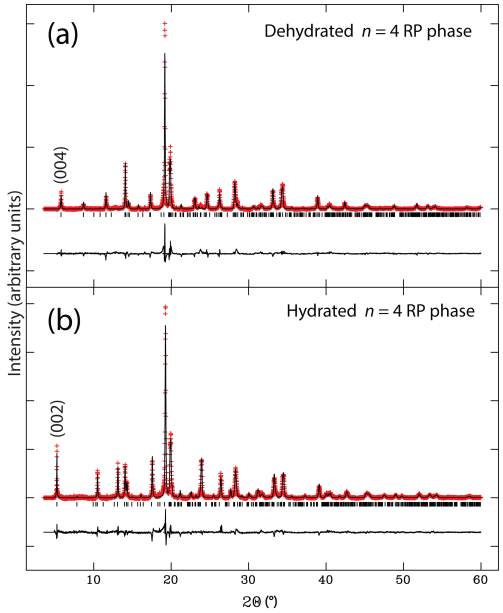

Figure 4: Room-temperature Rietveld refinements against SXRD patterns. Data are red crosses, overlayed with the calculated pattern on top as a black line and the difference curve underneath. Characteristic low-angle $(00l)$ peaks are labelled to illustrate the expansion of the stacking axis upon hydration. (a) The dehydrated phase in $Bb2_1m$ with refined lattice parameters $a = 5.5146(2)$, $b = 5.5449(2)$, $c = 37.7812(14)$ Å, V = 1155.28(13) Å^3. (b) The hydrated phase in $Pb2_1m$ with refined lattice parameters $a = 5.49977(13)$, $b = 5.52665(13)$, $c = 20.8566(5)$ Å, V = 633.94(4) Å^3. The fitting statistics for (b) are χ^2= 8.951, R_{wp} 0.0526 and R_p 0.0380.

The layered formula for RP phases indicates that there are two potassium ions in the interlayer per formula unit. Charge neutrality is maintained by doping K for Bi on the A-site

of the perovskite block, *i.e.*, the formula could be better written as $K_2[Bi_{2.5}K_{0.5}Ti_4O_{13}]$. This is analogous to K/Bi co-occupancy on the perovskite A-site of $K_{0.5}Bi_{0.5}TiO_3$ ($n = \infty$)[41,42] and Na/Ca on the A-sites of $Na_2Ca_2Nb_4O_{13}$.[39,40] Hence, site occupancy was also refined to determine if there was a preferred A-site for K/Bi co-occupancy. There are two distinct A-sites as shown in Figure 5: the two equivalent A-sites towards the outer perovskite block closer to the interlayer (A2); and the central/core A-site (A1). By Rietveld refinement a preference was observed for A2 to have mixed K/Bi occupancy, with the central A1 remaining purely as Bi (Figure 5). As the refined values were close to the neutral composition supporting our EDX results, the A2 site was fixed as 0.25K:0.75Bi and the A1 site as 1.0 Bi.

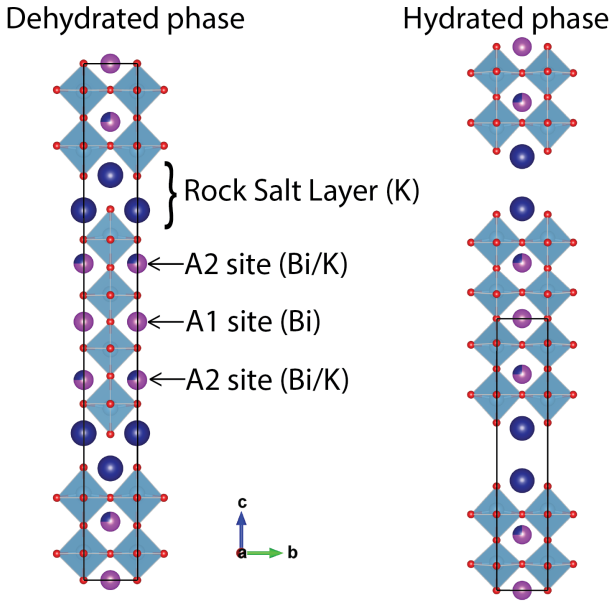

Figure 5: A simplified drawing of the $n = 4$ RP phase in its dehydrated form (left) and hydrated form (right). Blue polyhedra represent TiO_6 octahedra with purple Bi atoms in the A-site. K is represented in dark blue. Unit cell boundaries are outlined as black boxes. Refinements show that A2 is a mixed K/Bi while A1 is purely Bi.

As shown in Figure 4, upon hydration there is a typical *c*-axis expansion observed by a shift of (00*l*) peaks to lower 2θ values. In addition, new peaks are observed for the hydrated sample, indicative of a change from body-centered I (dehydrated phase) to primitive P (hydrated phase). This removes the staggered offset of the rock salt structure between adjacent perovskite layers in the dehydrated structure and halves the *c*-axis of the unit

cell. Preliminary Rietveld refinements against SXRD data for the hydrated phase produced a stable P structure with a significant gap between layers (Figure 5 right), which is the presumed location of intercalated water.[27] Although hydration is reported to occur in many RP phases, interlayer re-centering is not observed in all hydrated RP phases.[27,43] The water between the layers is assumed to be disordered.[44,45] An appropriate model was constructed in the $Pb2_1m$ space group based off of the original $Bb2_1m$. Due to the insensitivity of SXRD for lighter elements, the hydrated model was refined with an interlayer gap (no H_2O molecules present). Refinements in $Pmmm$ did not account for the split peaks at $\sim$20° 2θ and failed to converge. The statistics and Rietveld fit for the hydrated phase are shown in Figure 4(b). Refining for A-site occupancies with this model for $K_{2.5}Bi_{2.5}Ti_4O_{13} \cdot H_2O$ show that K/Bi A-site preferences do not change, preserving the cation disorder in this system, as expected given the mild condiction of (de)hydration.

The unit cell parameters reported in the caption of Figure 4 for both the dehydrated and hydrated phases are in good agreement with what was previously reported by Gopalakrishnan *et al.*[28]

Phase Transition Behaviour

Many perovskite-type materials with d^0 cations octahedrally coordinated by oxygen have been investigated for ferroelectric characteristics which can also be present in RP phases. The room-temperature structures of both the dehydrated and hydrated $n = 4$ RP phases were best modelled using $Bb2_1m$ and $Pb2_1m$ (polar) rather than $Immm$ and $Pmmm$ (non-polar) respectively, suggestive of ferroelectric behaviour. *In situ* SXRD diffraction studies revealed that the lattice parameters a and b converge in a continuous manner (Figure 6), indicative of a second-order phase transition to a higher symmetry tetragonal phase, $I4/mmm$. Sequential Rietveld refinements were carried out for lattice parameters, peak profile, zero offsets, background and globally constrained isotropic ADPs for each temperature step. By plotting the orthorhombic distortion $(\frac{b}{a} - 1)$ as an order parameter as shown in Figure 6,

we observe that the transition is broad (shown by the plateauing of the order parameter at higher temperatures) indicative of a relaxor-type transition.[46] The derivative of the order parameter (not shown) points to a T_C of approximately 600 °C. Interestingly, perovskite-type $K_{0.5}Bi_{0.5}TiO_3$ has been shown to display relaxor-type behaviour with a broad structural transition and peak in the dielectric constant at 410 °C.[42,47]

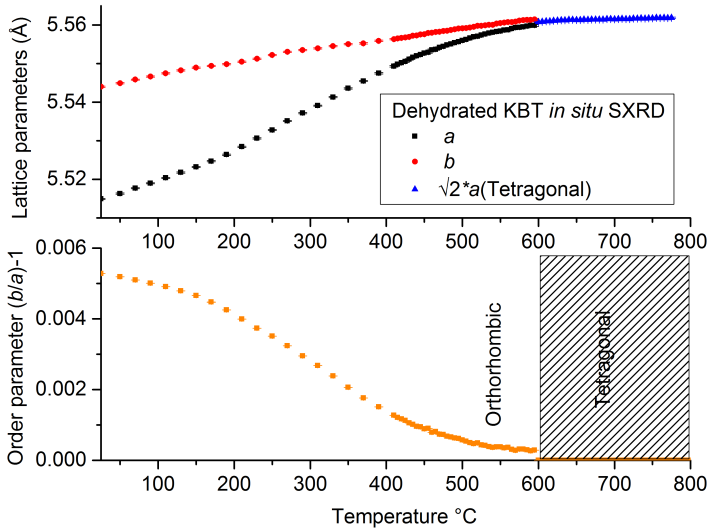

Figure 6: Extracted lattice parameters from sequential Rietveld refinements of $K_{2.5}Bi_{2.5}Ti_4O_{13}$. The circles and squares represent the a and b lattice parameters of $K_{2.5}Bi_{2.5}Ti_4O_{13}$ respectively, converging in the tetragonal $I4/mmm$ phase (blue triangle).

Relaxor ferroelectrics, compared to conventional ferroelectrics, have ferroelectric domains distributed across polar-nano-regions (PNRs), which transform at different temperatures, resulting in a broad transition.[46] $K_{0.5}Bi_{0.5}TiO_3$ was confirmed by *in situ* SXRD to have a broad T_C of approximately 410 °C.[42,47] $K_{2.5}Bi_{2.5}Ti_4O_{13}$ appears to have a significantly higher T_C, indicative of a more distorted structure and implying enhanced ferroelectricity in the low dimensional structure. Investigations in physical properties in relation to T_C are discussed later in this article.

We used *in situ* diffraction methods to track changes in atomic structure associated with the dehydration process observed by TGA. Figure 7 shows *in situ* SXRD data of a hydrated sample heated from room temperature. The dehydrated phase completely dominates the

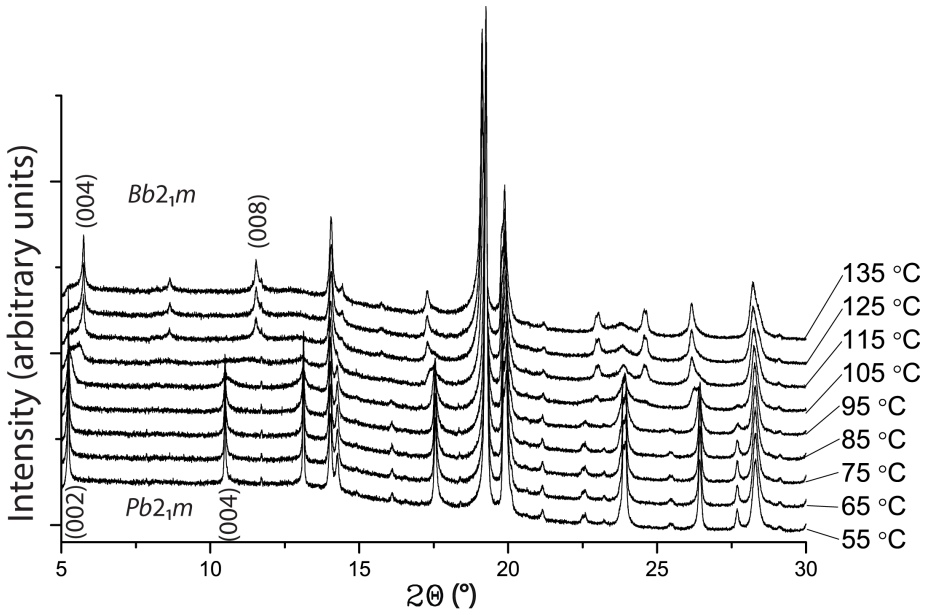

Figure 7: Tracking the dehydration process of $K_{2.5}Bi_{2.5}Ti_4O_{13} \cdot H_2O$ with SXRD.

pattern above 115 °C, in good agreement with TGA. The sample shows good crystallinity after dehydration, in contrast to reports for Sr-containing RP phases, which show significant decomposition to $SrTiO_3$ and $SrCO_3$.[27] The dehydration in $K_{2.5}Bi_{2.5}Ti_4O_{13}$ appears to be first-order, as expected given the reconstructive nature of the transition. A slight broadening of hydrated phase peaks is evident in the 95 °C pattern in Figure 7, presumably due to the loss of interlayer order following partial dehydration. After dehydration, the sample behaves similarly to the original dehydrated $K_{2.5}Bi_{2.5}Ti_4O_{13}$ discussed above.

Local Hydration Environment

A number of RP phases have been shown to hydrate at room temperature and pressure, and in the present work, we have shown that $K_{2.5}Bi_{2.5}Ti_4O_{13}$ incorporates one water molecule and changes from a body-centered (I) to a primitive (P) unit cell. In order to contribute to the search for new materials for photocatalytic activity and potential proton conduction, it is important to identify the atomic environment of the interlayer in the hydrated phase. Of particular interest is the question of whether the phase contains intact H_2O molecules, or is hydroxylated, *i.e,* contains OH^- anions.

It is known that the photocatalytic behaviour is enhanced in layered materials.[15] However, in the RP phases, crystal interactions with water have not been thoroughly investigated. Generally, intercalated intact water molecules are assumed to be in a disordered state with the oxygen atoms of interstitial H_2O directly underneath apical perovskite oxygen atoms.[12,13,44] However, the reconstructive transition of the layers upon hydration suggests that the H atoms of H_2O molecules also have strong interactions with the perovskite layer and might possibly be ordered in RP phases.

We attempted to resolve the hydration environment at room temperature experimentally for $K_{2.5}Bi_{2.5}Ti_4O_{13} \cdot H_2O$ using NPD. Low-temperature (100 K) NPD patterns were collected in the hope of "freezing" the hydrated structure. Figure 9(a) shows a three-dimensional difference Fourier map of the hydrated structure for a model containing no water, close to its expected location. Peaks due to positive (O) and negative (H) nuclear scattering are clearly resolved, with water molecules in a vertical orientation that suggests hydrogen bonds to apical oxygen atoms of the TiO_6 octahedra. H_2O positions were refined in the low-temperature condition while constraining the isotropic ADPs of the water molecule to be equal (Figure 9(b)). The 100 K model was used as the starting model for the 300 K refinement. The isotropic ADPs were refined but the H_2O positions were fixed in this case. The inclusion of water in the orientation inferred by our difference Fourier map significantly improved the fitting statistics versus an interlayer gap as shown in Table 3, yielding relatively high ADPs for water specifically (the refined U_{iso} values for H_2O at 100 K is 0.106(15), and 300 K is 0.122(14)). A list of full phase parameters are found in the supplementary CIF files. Final fits are shown in Figure 8.

Table 3: Fitting parameters extracted from NPD Rietveld refinements showing an improvement by including a water molecule in the models.

	100 K		300 K	
Parameter	Interlayer Gap	Included H_2O	Interlayer Gap	Included H_2O
χ^2	1.359	1.211	1.694	1.244
R_{wp}	0.0246	0.0231	0.0273	0.0234
R_p	0.0194	0.0182	0.0211	0.0183

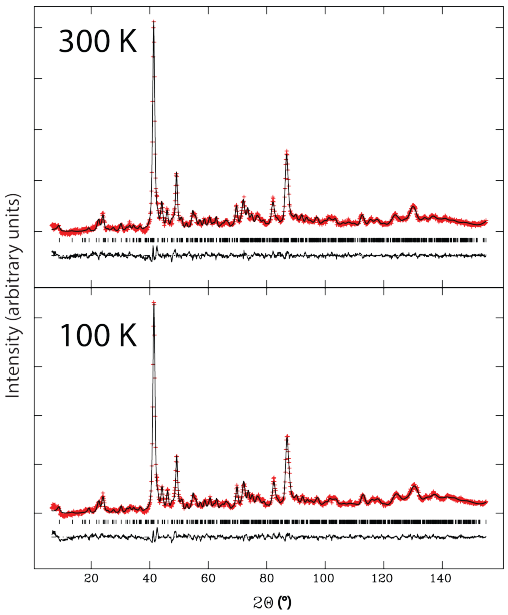

Figure 8: Rietveld refined fit against NPD data for the hydrated phase at 100 K and 300 K in the $Pb2_1m$ space group. The refined lattice parameters at 100 K are $a = 5.4979(18)$, $b = 5.5175(17)$, $c = 20.688(4)$ Å, V = 627.6(3) Å^3 and at 300 K are $a = 5.5066(17)$, $b = 5.5261(17)$, $c = 20.758(5)$ Å, V = 631.7(3) Å^3.

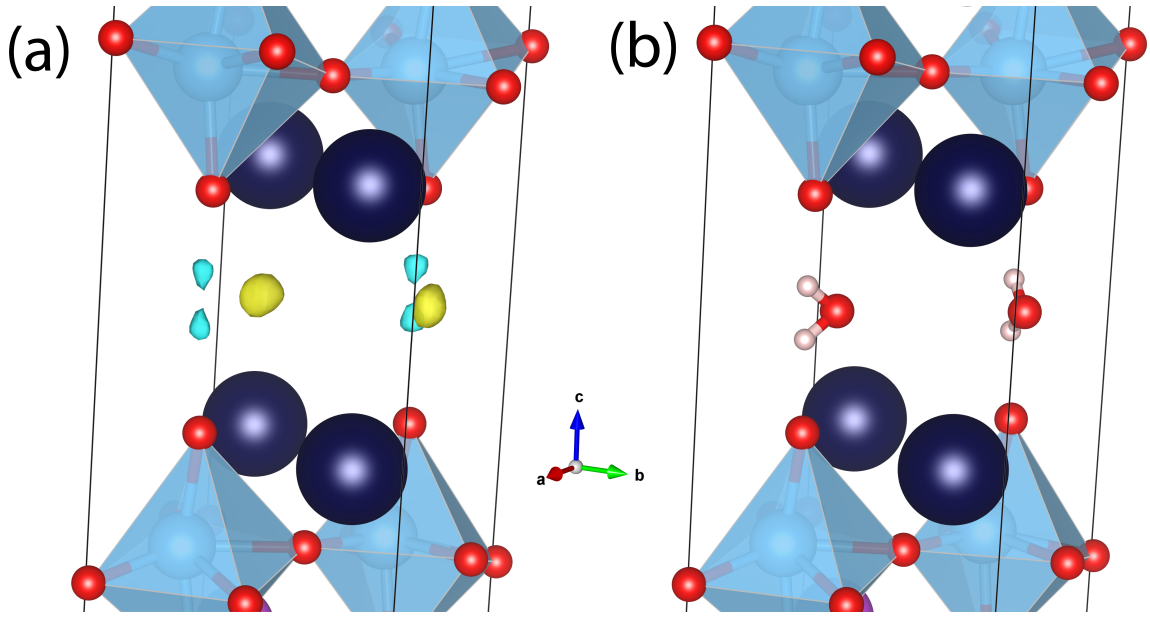

Figure 9: (a) shows the difference Fourier map of the 100 K NPD Rietveld refined structure for $K_{2.5}Bi_{2.5}Ti_4O_{13} \cdot H_2O$ with no water included. Yellow peaks are positive and blue peaks are negative. (b) is the final refined hydrated structure at 100 K inclusive of water.

Possible water coordination environments were also evaluated by DFT calculations. A

unit cell was constructed of high symmetry (*Pmmm*) to simplify the model for visualisation and modifications. The cell was doubled along a and b to accommodate up to four water molecules (a fully hydrated crystal) in different local orientations. The mixed K/Bi site A2 was assumed to be fully occupied by Bi. Initial geometry optimisation (GO) tests started with split water (ions H^+ and OH^-) among interstitial sites. However, intact water molecules reformed, suggesting that those represent the lower energy state: *i.e.*, the results suggest $K_{2.5}Bi_{2.5}Ti_4O_{13} \cdot H_2O$ rather than a hydroxylated phase.

A feature of the GO structure was the apparent presence of hydrogen bonds from the positive dipole of water to the apical oxygens of the edge of only one perovskite block. This is different to the orientation suggested by our difference Fourier map discussed above, prompting a more detailed investigation into water orientation and behaviour. If water were to exist as a molecular species, then its dipole orientation may be important in understanding enhanced polarisation or the driving force for crystal re-centering in the observed RP phases. Preliminary molecular dynamics (MD) calculations were performed at varying temperatures with different amounts of water in orientations suggested by GO.

Feasible low-energy superstructures were then created using the same doubled unit cell in a and b (2x2x1) in *Pmmm*. One set of models consisted of the water molecules hydrogen bonding in a "v"-shaped manner forming hydrogen bonds to apical oxygens and bridging across A-sites of the rock salt layer. The lowest energy form of this model had water molecules arranged in an alternate up-down fashion in the *ab*-plane (shown in Figure 10(a)). The second set of models had the water molecules in vertical orientations ("pillared"). A lower energy converged with some of the "pillared" water molecules orthogonal to their nearest neighbours in the *ab*-plane, bridging between perovskite blocks (shown in Figure 10(b)) modelling a disordered water environment. This indicates that water molecules do not have a preference to all align along either the a or b axes, and in the real structure are probably randomly aligned.

The calculated ground state energies from GO calculations showed that the "pillared"

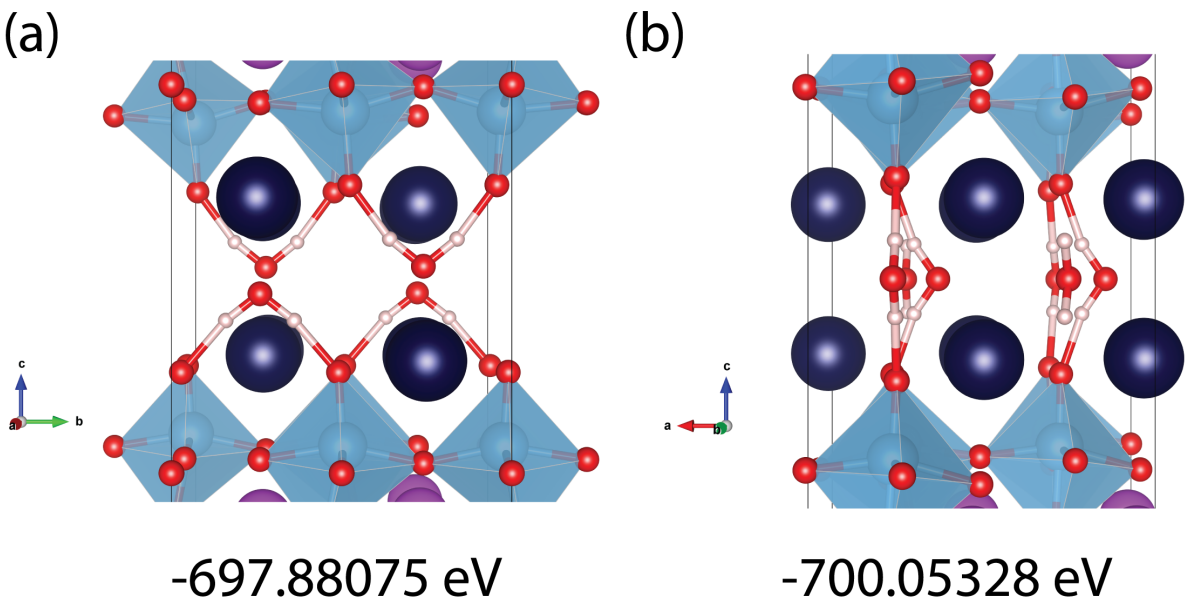

Figure 10: The lowest energy forms of the fully hydrated structure, from GO calculations. (a) Water molecules hydrogen bonding in a "v"-shaped manner forming hydrogen bonds to apical oxygens and bridging across between A-sites of the rock salt layer. (b) Water in a vertical orientation ("pillared") pointing in the same or different directions relative to each other.

water model has a significantly lower energy ground state (∼2.17 eV or 21.7 meV/atom difference). The energetically favoured pillaring of water closely resembles our difference Fourier maps and refined structures above (Figure 9(b)).

Despite the result that vertically "pillared" H_2O represents the most probable ground state of the system, Rietveld refinements including this water configuration against NPD data still failed to converge. This suggests that the actual water configuration is disordered, either statically or dynamically. In order to test for potential splitting of water into ions in a dynamical process (important for photocatalytic and proton conduction mechanisms), water dynamics were investigated by MD simulations beginning with our GO supercells of $K_{2.5}Bi_{2.5}Ti_4O_{13} \cdot H_2O$. MDs were calculated with 1 fs time-steps over a 20 ps trajectory at 100, 298, 363 and 673 K.

The ellipsoids in Figure 11 represent the space explored by water molecules over the course of a given MD run with a semi-ordered water environment. At room temperature and

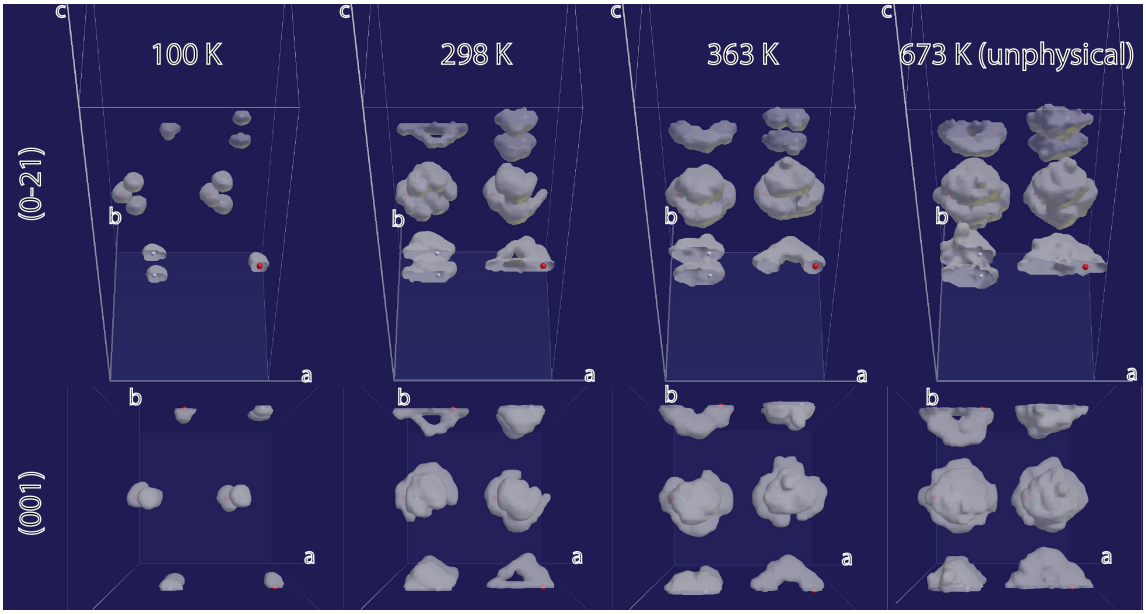

Figure 11: Extracted ellipsoids of the water molecules only with increasing temperatures from left to right. Top row is a view along (0-21) showing the progressive increase in ellipsoid volume with temperature. Bottom row consists of corresponding projections along (001) showing the rotations about the c-axis of "pillared" water.

above, the system has enough heat to overcome an energy barrier allowing observable water rotations about the c-axis suggesting that this motion has a relatively small energy cost. At the (physically unrealistic) temperature of 673 K there is enough thermal vibration for water to freely rotate while water molecules remain intact and H-bonded to apical oxygens. The incomplete rotation of ellipsoid clouds at 298 and 363 K in the projection along the (001) plane suggests either geometrical constraints due to an orthorhombic unit cell ($a \neq b$), or the limitations of running simulations in a finite unit cell. Further investigations using more complex MD models and quasi-elestic neutron scattering are underway.

Dielectric Measurements

All structural models for this $n = 4$ RP phase have been supported by improved statistical fits in Rietveld refinements with a polar space group, fundamental to ferroelectric properties. Conventional methods to test for ferroelectricity failed due to the requirement of ultra-dense pellets ($\geq$ 95%), which could not be prepared ($K_{2.5}Bi_{2.5}Ti_4O_{13} \cdot H_2O$ cannot be sintered

without dehydrating). Thus, dielectric properties for a fully hydrated sample were probed. This will provide valuable information on its conduction behaviour and dynamic polarisation *in situ*.

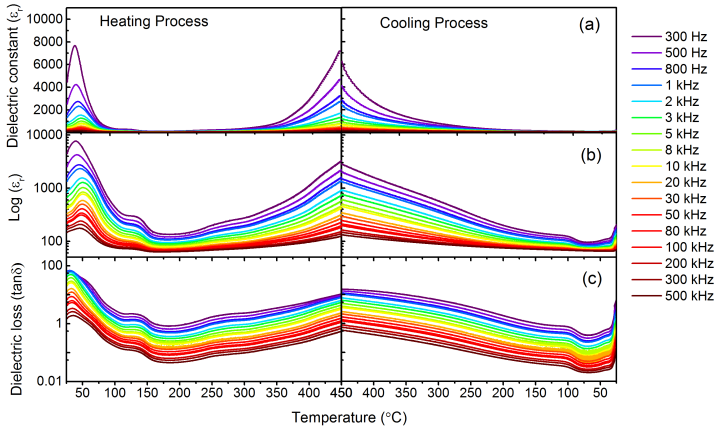

Figure 12: Dielectric measurements of a pelletised $K_{2.5}Bi_{2.5}Ti_4O_{13} \cdot H_2O$ with gold paste electrodes at various frequencies with increasing temperature. (a) The temperature dependent plot of the dielectric constant (ϵ_r) versus temperature, shown on a logarithmic scale in (b), and (c) the logarithm scale of the dielectric loss (tanδ).

Our first observation in Figure 12(a), is the large dielectric constant at room temperature and at high temperature. The logarithmic scale (Figure 12(b)) highlights three peaks in the temperature-dependent dielectric spectra. The first peak in the vicinity of room temperature corresponds to two different polarisation mechanisms (that cannot be de-convoluted) which can be related to water mobility by a frequency dependent shift (300 Hz - 500 kHz). The dielectric curves below 50 °C can be assigned to absorbed surface water (slight weight loss in TGA, see Figure 3) and those below 110 °C to crystalline water. The presence of water causes a considerable increase in both dielectric constant (ϵ_r) and loss (tanδ). This is much higher than for its perovskite-type counterparts because polar water is capable of aligning itself under an applied electric field making a large contribution to ϵ_r. Such an alignment also dynamically affects the electron state density distribution of surrounding atoms and

subsequently changes the polarization. During the heating process, the water molecule will migrate significantly (dehydration), which corresponds to the rapid decrease of ϵ_r and tanδ. The temperature at which this structural transition occurs is in good agreement with TGA and *in situ* SXRD results shown above, corresponding to the second transition in dielectric measurements from ∼110 °C to ∼200 °C visible on the logarithmic scale. This feature appears to be reversible as it is also apparent in the cooling curve, but as a smaller feature and at a lower temperature. This may indicate the start of the slow hydration process at the surface of the sample and hysteretic behaviour in hydration/dehydration temperature. Above 200 °C, a small shoulder is observed at 250 °C during the heating process, but this is not obvious on cooling. This may be related to irreversible ionic defects such as small oxygen vacancies in the structure[27] post crystal reconstruction, increasing ionicity.

Above 250 °C we see a continual increase in both ϵ_r and tanδ up to the limit of the gold electrode (∼500 °C). Although the dielectric constant follows the same trend with different frequencies, tanδ (dielectric loss), shows less frequency-dependence, presenting an almost plateauing behaviour as the temperature approaches the high-temperature structural phase transition as determined by structural refinements. This suggest two possible contributions to the observed dielectric behaviours in the high-temperature range: polarisation due to ionic migration due to the increased heat in the system; and polarisation originating from the broad, phase transition, which is consistent with the proposed relaxor nature of the material determined by *in situ* diffraction measurements. These two mechanisms compete against each other, with the structural phase transition dominating as the temperature approaches T_C, minimising the further increase of the dielectric loss arising from the ionic migration contribution. To elucidate the high-temperature transition, a sintered sample with Pd-Ag paste was measured up to synthetic temperatures (∼750 °C). The completion of the high-temperature transition is shown in Figure 13 at ∼ 600 °C, which is broad indicative of relaxor behaviour as suggested by our *in situ* diffraction results.

The relaxor nature of the structural phase transition is reminiscent of the closely re-

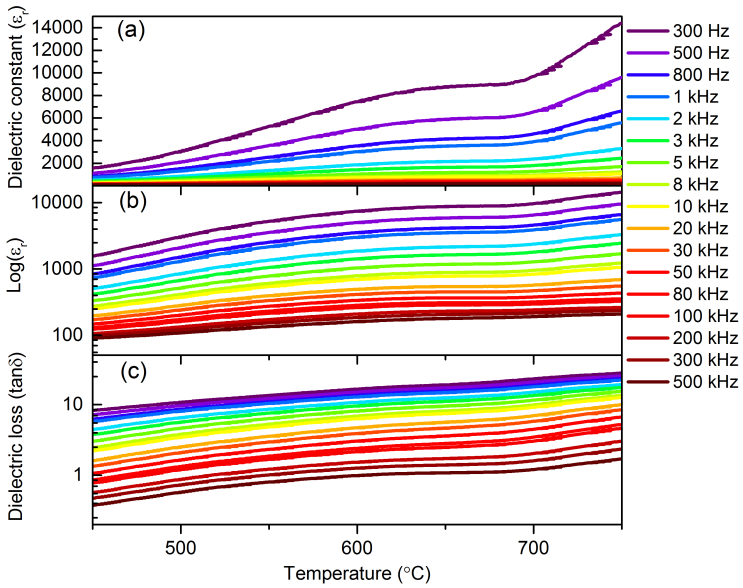

Figure 13: Dielectric measurements of a pelletised $K_{2.5}Bi_{2.5}Ti_4O_{13}$ with Pd-Ag paste electrodes at various frequencies with increasing temperature. (a) The temperature dependent plot of the dielectric constant (ϵ_r) versus temperature, shown on a logarithmic scale in (b), and (c) the logarithm scale of the dielectric loss (tanδ).

lated perovskite $K_{0.5}Bi_{0.5}TiO_3$ discussed earlier in relation to the *in situ* diffraction analysis above.[42,47] For *in situ* diffraction and the current dielectric measurements, the T_C for $K_{2.5}Bi_{2.5}Ti_4O_{13}$ is significantly higher than the perovskite with a corresponding ϵ_r of ~3000 at 1 kHz, which is remarkably close to the perovskite $K_{0.5}Bi_{0.5}TiO_3$ fo rthe same frequency range.[47] This finding is contrary to other studies on layered perovskite phases where the T_C for perovskite compounds is significantly higher. Ferroelectric layered perovskites minimise the cooperative interaction of oxygen octahedra perpendicular to the perovskite layers due to the disruptive presence of their interlayer space, which is important for ferroelectric ordering. Increasing the number of layers (from $n = 1$) increases this cooperative effect, favouring ferroelectric properties, which should therefore be largest in the $n = \infty$ compound.[48,49] Studies have shown that as n values increase, so do the relative dielectric constants, with $n = \infty$ having the largest response.[2,49] In order to explain our result, one must consider the structural composition of the perovskite-only environment in both $n = 4$ and ∞.

On average, the perovskite layer in the RP phase (when calculated using a unit cell

from one outer TiO_6 octahedron to another), has 0.625 Bi per Ti, whereas the perovskite has 0.5 Bi per Ti. The RP phase is able to accommodate a higher Bi:Ti ratio due to its structural flexibility in compensating for charge neutrality elsewhere in the unit cell (rock salt-type layers). Due to the asymmetric nature of the Bi^{3+} cation, the perovskite block in the RP phase would exhibit enhanced distortions compared to the pure perovskite phase hence an observed higher T_C despite the latter having enhanced oxygen cooperative effects. However, comparing the two materials across common frequencies present in this work and those measured by Bengagi *et al.*,[47] it appears that at increasing frequencies, the layered ϵ_r rapidly diminishes whereas the perovskite decreases relatively slightly. This appears as a dynamical lag exhibited by the layered structure and can be explained by a lack of the three dimensional cooperative phonons in $K_{2.5}Bi_{2.5}Ti_4O_{13}$.

Conclusion

A new highly ordered Bi-containing Ruddlesden-Popper phase, $K_{2.5}Bi_{2.5}Ti_4O_{13}$, has been prepared by solid state synthesis. It has been shown to readily uptake precisely one water molecule per formula unit at room temperature and pressure (accelerated under humid atmospheres) forming $K_{2.5}Bi_{2.5}Ti_4O_{13} \cdot H_2O$. Both phases have been characterised by Rietveld refinement against high-resolution synchrotron and neutron powder diffraction data, which show that the structure consists of a quadruple stacked ($n = 4$) perovskite layer with K-ions occupying the rock salt layer and its next nearest A-site. The hydrated sample was shown to remove the offset of adjacent perovskite layers present in the dehydrated sample. Using *ab initio* computational methods, we have shown that the water environment consists of intact water molecules in a vertical "pillared" arrangement bridging across the interlayer space. This is supported by difference Fourier maps in low-temperature neutron diffraction refinements. Rotations of water molecules about the *c*-axis were evident in molecular dynamics calculations, which increased in rotation angle with increasing temperature. *In*

situ diffraction methods point to a broad structural phase transition consistent with relaxor behaviour from orthorhombic to tetragonal at T_C ~600 °C. A corresponding broad transition in the dielectric constant was observed in impedance spectroscopy measurements. This Ruddlesden-Popper structure displays a higher T_C compared to its perovskite analogue due to its relative Bi-rich composition in the perovskite unit. The dielectric constant appears to rapidly decrease with increasing frequency due to a lack of three-dimensionality. It is also evident that water has a significant contribution to the dielectric constant, which disappears after dehydration. Further investigations in potential proton conduction measurements and deuteration experiments are considered for extending this work. Photocatalytic properties of this $n = 4$ RP phase has not been tested, although a closely related $n = 5$ DJ phase has been investigated.[29] This work along with other hydrous metal oxide materials may well be worth pursuing further in light of the structural results presented here. Future studies are underway to apply similar investigative methods to other hydrated RP compounds.

Acknowledgement

The authors thank the Australian Research Council-Discovery Projects (DP150102863). This work was, in part, performed at the powder diffraction beamline at the Australian Synchrotron with assistance from beamline scientists and Drs Helen Brand and Justin Kimpton. The authors acknowledge the facilities, and the scientific assistance of the Australian Microscopy & Microanalysis Research Facility at the Australian Centre of Microscopy & Microanalysis, The university of Sydney. This work was supported by the Dr Joan R. Clarke Scholarship.

Supporting Information Available

Figure S1, SHG document and Crystallographic Information Files (CIFs) for refined structures $K_{2.5}Bi_{2.5}Ti_4O_{13}$ and $K_{2.5}Bi_{2.5}Ti_4O_{13} \cdot H_2O$ at room-temperature and $K_{2.5}Bi_{2.5}Ti_4O_{13} \cdot H_2O$

at 100 K.

References

(1) Subbarao, E. *Journal of Physics and Chemistry of Solids* **1962**, *23*, 665–676.

(2) Li, B.-W.; Osada, M.; Ebina, Y.; Ozawa, T. C.; Ma, R.; Sasaki, T. *Applied Physics Letters* **2010**, *96*.

(3) Jantsky, L.; Okamoto, H.; Thomas, M.; Karen, P.; Hauback, B. C.; Rosseinsky, M. J.; Fjellvag, H. *Chemistry of Materials* **2014**, *26*, 886–897.

(4) Bednorz, J.; Müller, K. *Zeitschrift für Physik B Condensed Matter* **1986**, *64*, 189–193.

(5) Wu, M.; Ashburn, J.; Torng, C.; Hor, P.; Meng, R.; Gao, L.; Huang, Z.; Wang, Y.; Chu, C. *Physical Review Letters* **1987**, *58*, 908–910.

(6) Maeno, Y.; Hashimoto, H.; Yoshida, K.; Nishizaki, S.; Fujita, T.; Bednorz, J.; Lichtenberg, F. *Nature* **1994**, *372*, 532–534.

(7) Ogino, H.; Matsumura, Y.; Katsura, Y.; Ushiyama, K.; Horii, S.; Kishio, K.; Shimoyama, J.-i. *Superconductor Science & Technology* **2009**, *22*.

(8) Sharma, N.; Ling, C. D.; Wrighter, G. E.; Chen, P. Y.; Kennedy, B. J.; Lee, P. L. *Journal of Solid State Chemistry* **2007**, *180*, 370–376.

(9) Sharma, N.; Kennedy, B. J.; Elcombe, M. M.; Liu, Y.; Ling, C. D. *Journal of Physics-Condensed Matter* **2008**, *20*.

(10) Liu, S.; Miiller, W.; Liu, Y.; Avdeev, M.; Ling, C. D. *Chemistry of Materials* **2012**, *24*, 3932–3942.

(11) Takata, T.; Furumi, Y.; Shinohara, K.; Tanaka, A.; Hara, M.; Kondo, J. N.; Domen, K. *Chemistry of Materials* **1997**, *9*, 1063–1064.

(12) Yao, W.; Ye, J. *Chemical Physics Letters* **2007**, *435*, 96–99.

(13) Shimizu, K.; Tsuji, Y.; Hatamachi, T.; Toda, K.; Kodama, T.; Sato, M.; Kitayama, Y. *Physical Chemistry Chemical Physics* **2004**, *6*, 1064–1069.

(14) Rodionov, I. A.; Silyukov, O. I.; Utkina, T. D.; Chislov, M. V.; Sokolova, Y. P.; Zvereva, I. A. *Russian Journal of General Chemistry* **2012**, *82*, 1191–1196.

(15) Kudo, A.; Miseki, Y. *Chemical Society Reviews* **2009**, *38*, 253–278.

(16) Auckett, J. E.; Studer, A. J.; Pellegrini, E.; Ollivier, J.; Johnson, M. R.; Schober, H.; Miiller, W.; Ling, C. D. *Chemistry of Materials* **2013**, *25*, 3080–3087.

(17) Uma, S.; Raju, A. R.; Gopalakrishnan, J. *J. Mater. Chem.* **1993**, *3*, 709–713.

(18) Schaak, R.; Mallouk, T. *Journal of Solid State Chemistry* **2000**, *155*, 46–54.

(19) Sato, M.; Kono, Y.; Jin, T. *Nippon Seramikkusu Kyokai Gakujutsu Ronbunshi-Journal of the Ceramic Society of Japan* **1993**, *101*, 980–984.

(20) Dion, M.; Ganne, M.; Tournoux, M. *Materials Research Bulletin* **1981**, *16*, 1429–1435.

(21) Ruddlesden, S.; Popper, P. *Acta Crystallographica* **1957**, *10*, 538–540.

(22) Aurivillius, B. *Arkiv For Kemi* **1950**, *1*, 499–512.

(23) Catalan, G.; Scott, J. F. *Advanced Materials* **2009**, *21*, 2463–2485.

(24) Seshadri, R.; Hill, N. *Chemistry of Materials* **2001**, *13*, 2892–2899.

(25) Fang, P.; Robbins, C.; Aurivillius, B. *Physical Review* **1962**, *126*, 892–&.

(26) Liu, S.; Blanchard, P. E. R.; Avdeev, M.; Kennedy, B. J.; Ling, C. D. *Journal of Solid State Chemistry* **2013**, *205*, 165–170.

(27) Lehtimaki, M.; Yamauchi, H.; Karppinen, M. *Journal of Solid State Chemistry* **2013**, *204*, 95–101.

(28) Gopalakrishnan, J.; Sivakumar, T.; Thangadurai, V.; Subbanna, G. *Inorganic Chemistry* **1999**, *38*, 2802–2806.

(29) He, C.-H.; Yang, O.-B. *Industrial & Engineering Chemistry Research* **2003**, *42*, 419–425.

(30) Wallwork, K. S.; Kennedy, B. J.; Wang, D. The high resolution powder diffraction beamline for the Australian Synchrotron. Synchrotron Radiation Instrumentation, Pts 1 and 2. 2 Huntington Quadrangle, STE 1NO1, Melville, NY 11747-4501 USA, 2007; pp 879–882, 9th International Conference on Synchrotron Radiation Instrumentation (SRI 2006), Daegu, South Korea, May 28-Jun 02, 2006.

(31) Liss, K.-D.; Hunter, B.; Hagen, M.; Noakes, T.; Kennedy, S. *Physica B-Condensed Matter* **2006**, *385-86*, 1010–1012.

(32) Larson, A.; Dreele, R. V. General Structure Analysis System (GSAS). 2000.

(33) Toby, B. *Journal of Applied Crystallography* **2001**, *34*, 210–213.

(34) Momma, K.; Izumi, F. *Journal of Applied Crystallography* **2008**, *41*, 653–658.

(35) Kresse, G.; Furthmuller, J. *Computational Materials Science* **1996**, *6*, 15–50.

(36) Kresse, G.; Joubert, D. *Physical Review B* **1999**, *59*, 1758–1775.

(37) Perdew, J.; Burke, K.; Ernzerhof, M. *Physical Review Letters* **1996**, *77*, 3865–3868.

(38) Richard, D.; Ferrand, M.; Kearley, G. *J. Neutron Research* **1996**, *9*, 33–39.

(39) Chiba, K.; Ishizawa, N.; Nagai, Y.; Oishi, S. *Solid State Ionics* **1998**, *108*, 179–183, IUMRS-ICA Symposium R on Perovskite-Related Oxides - Preparation, Properties and Perspectives, Chiba, Japan, Sep 16-17, 1997.

(40) Chiba, K.; Ishizawa, N.; Oishi, S. *Acta Crystallographica Section C-Crystal Structure Communications* **1999**, *55*, 1041–1044.

(41) Otonicar, M.; Skapin, S. D.; Jancar, B.; Ubic, R.; Suvorov, D. *Journal of the American Ceramic Society* **2010**, *93*, 4168–4173.

(42) Liu, S.; Blanchard, P. E. R.; Zhang, Z.; Kennedy, B. J.; Ling, C. D. *Dalton Trans.* **2015**, *44*, 10681–10688.

(43) Lehtimaki, M.; Hirasa, A.; Matvejeff, M.; Yamauchi, H.; Karppinen, M. *Journal of Solid State Chemistry* **2007**, *180*, 3247–3252.

(44) Toda, K.; Kameo, Y.; Kurita, S.; Sato, M. *Bulletin of the Chemical Society of Japan* **1996**, *69*, 349–352.

(45) Kodenkandath, T.; Wiley, J. *Materials Research Bulletin* **2000**, *35*, 1737–1742.

(46) Cross, L. *Ferroelectrics* **1987**, *76*, 241–267.

(47) Bengagi, M.; Morini, F.; El Maaoui, M.; Marchet, P. *Physica Status Solidi A-Applications and Materials Science* **2012**, *209*, 2063–2072.

(48) Sohn, J.; Inaguma, Y.; Itoh, M.; Nakamura, T. *Materials Science and Engineering B-Solid State Materials for Advanced Technology* **1996**, *41*, 50–54, 2nd International Symposium on Oxide Electronics, Yokohama, Japan, DEC 14-15, 1995.

(49) Kamba, S.; Samoukhina, P.; Kadlec, F.; Pokorny, J.; Petzelt, J.; Reaney, I.; Wise, P. *Journal of the European Ceramic Society* **2003**, *23*, 2639–2645, International Conference on Microwave Materials and Their Applications (MMA 2002), York, England, Sep 01-03, 2002.

This material is available free of charge via the Internet at `http://pubs.acs.org/`.